

Design of Metal-Halide Inverse-Hybrid Perovskites

Julian Gebhardt, and Andrew M. Rappe

J. Phys. Chem. C, **Just Accepted Manuscript** • DOI: 10.1021/acs.jpcc.8b01008 • Publication Date (Web): 13 Mar 2018

Downloaded from <http://pubs.acs.org> on March 22, 2018

Just Accepted

"Just Accepted" manuscripts have been peer-reviewed and accepted for publication. They are posted online prior to technical editing, formatting for publication and author proofing. The American Chemical Society provides "Just Accepted" as a service to the research community to expedite the dissemination of scientific material as soon as possible after acceptance. "Just Accepted" manuscripts appear in full in PDF format accompanied by an HTML abstract. "Just Accepted" manuscripts have been fully peer reviewed, but should not be considered the official version of record. They are citable by the Digital Object Identifier (DOI®). "Just Accepted" is an optional service offered to authors. Therefore, the "Just Accepted" Web site may not include all articles that will be published in the journal. After a manuscript is technically edited and formatted, it will be removed from the "Just Accepted" Web site and published as an ASAP article. Note that technical editing may introduce minor changes to the manuscript text and/or graphics which could affect content, and all legal disclaimers and ethical guidelines that apply to the journal pertain. ACS cannot be held responsible for errors or consequences arising from the use of information contained in these "Just Accepted" manuscripts.



ACS Publications

is published by the American Chemical Society, 1155 Sixteenth Street N.W., Washington, DC 20036

Published by American Chemical Society. Copyright © American Chemical Society. However, no copyright claim is made to original U.S. Government works, or works produced by employees of any Commonwealth realm Crown government in the course of their duties.

1
2
3
4
5
6
7
8
9
10
11
12
13
14
15
16
17
18
19
20
21
22
23
24
25
26
27
28
29
30
31
32
33
34
35
36
37
38
39
40
41
42
43
44
45
46
47
48
49
50
51
52
53
54
55
56
57
58
59
60

Design of Metal-Halide Inverse-Hybrid Perovskites

Julian Gebhardt* and Andrew M. Rappe

*Department of Chemistry, University of Pennsylvania, Philadelphia, Pennsylvania
19104-6323, United States*

E-mail: jugeb@sas.upenn.edu

Abstract

We recently introduced a new class of perovskites, with inorganic anions on the *A*- and *B*-sites and an organic cation on the *X*-site, the so called inverse-hybrid perovskites (IHPs). We found compounds that are predicted to be stable, possess large polarization, and span a wide range of electronic properties. Here, we present the materials search strategy that enabled these results. We demonstrate the design principles in terms of ion and site composition. Overall, we consider elements from most main groups of the periodic table, investigating their ability to form mono- or divalent anions in the framework of IHPs. We observe structural changes based on tolerance factor. Compounds are found in the perovskite or the related CaIrO_3 structure and different orientations of the employed organic cation (methylammonium), lead to different $B \cdots X \cdots B$ bridging motifs. Furthermore, we demonstrate how the perovskite structure can be favored by interchanging *B*- and *A*-site anions and adjusting the ions within groups of the periodic table accordingly. Besides chalcogenide halides, we find that elements of groups XIII to XV can successfully form mono- or divalent anions by partly filling their valence *p* shell. Spin-orbit coupling in the heavier elements leads to interesting electronic motifs. Furthermore, while light divalent elements show a tendency towards protonation, this is suppressed by employing heavier elements of the same group. Evaluating the stability of these novel compounds also requires to investigate largely unknown methylammonium compounds with mono- and divalent anions.

Introduction

We recently proposed a new class of functional hybrid-perovskite materials, the so-called inverse-hybrid perovskites (IHPs),¹ demonstrating their compositional flexibility, their variety in electronic structure, and the potential for ferroelectrics with very large polarization. Analogous to inverse (or anti) perovskites (IP),²⁻¹¹ IHPs have X_3BA structure containing a (here organic) cation on the *X*-site and two anions on the *A*- and *B*- sites. In this structure,

the covalent character of BX_6 octahedra in HPs is replaced by hydrogen bonding. Predominantly hydrogen-bonded perovskite structures are known from molecular double organic perovskites with organic cations on the A - and B -site,^{12,13} such as piperazinium dication ammonium chloride $(C_4H_{12}N_2)(NH_4)Cl_3$, which is stable up to 600 °C.¹² They are also found in HPs with organic A -site cations and X -site anions,^{14,15} and analogous polar bonds are found when X -site anions are combined with inorganic cations.^{16–18}

Herein, we show in detail our materials search to combine main group anions with small organic cations, mainly the intensively studied $CH_3NH_3^+$ (MA). As metal anions we consider monovalent ($a^- = F, Cl, Br, I$) and divalent ($a^{2-} = O, S, Se, \text{ and } Te$) anions. In addition we investigate the possibility of group XIII and XIV elements (Ga, Tl, Ge, Sn, and Pb) to form divalent anions and group XIII (Tl), XV (Bi), and alkali metals (Na and Rb) to form monovalent anions. We use estimated tolerance factors t as well as accurate density-functional calculations in our search for suitable, stable compounds. We find that perovskites form preferentially for $t > 0.76$. For smaller t , a reduced tilting of the MA molecules is preferred, leading to a different $B \cdots X \cdots B$ bridging motif. For most of these cases with $t < 0.76$, a different corner- and edge-sharing phase is more favorable. We investigate the site preference of ions and report the structural and electronic properties of the obtained stable compounds. The influence of spin-orbit coupling (SOC) and level of electronic structure theory is investigated for relevant systems. In addition, we demonstrate that IHPs generally have very high polarization. To estimate the stability of these novel compounds, we also investigate the phase stability of $(MA)_2a^{2-}$ and MAa^- reference compounds.

Computational Details

Structures were fully optimized by non-spin-polarized (unless noted otherwise) density-functional theory (DFT). We use the Perdew–Burke–Ernzerhof (PBE) generalized gradient approximation¹⁹ as implemented in the QUANTUM ESPRESSO package,²⁰ supplemented by

the D2 method²¹ in order to account for dispersive interactions. Core electrons are treated by norm-conserving, optimized, nonlocal, scalar-relativistic pseudopotentials generated with OPIUM.^{22–24} In cases where SOC plays an important role, a fully-relativistic treatment is employed to investigate the impact on the electronic structure. Wave functions are expanded in a plane-wave basis with an energy cutoff of 680 eV (and an increased basis of 885 eV for systems containing Rb). Total energies and atomic structures are fully relaxed to 10^{-7} eV/cell and until forces acting on ions are below 0.0025 eV/Å. The Brillouin zone is sampled by a $6\times 6\times 6$ Monkhorst-Pack \mathbf{k} -point grid,²⁵ whereas a denser grid of $18\times 18\times 18$ \mathbf{k} points is used for calculating the density of states (DoS). Initial structures are constructed as cubic perovskites for a unit cell with one formula unit (f.u.). As initial guess, we orient one MA ion along each spatial direction. The lattice dimensions are initially chosen to be large (7.5 Å), in order to allow for enough spatial freedom during structure optimization. These initial structures show perovskite or an edge- and corner-sharing structure (CaIrO_3) for most tested compositions. Consequently, we investigate the stability of compositions in these two phases. Reference structures (described below) for estimated binding energies are computed with a similar setup for $\text{MA}a^-$ and $(\text{MA})_2a^{2-}$ compounds. For nonmetallic, stable cases we compare the PBE with HSE06²⁶ results for a better quantitative estimate of the band gap. The Fock operator for the HSE06 calculation is represented on a $3\times 3\times 3$ \mathbf{q} point grid using a kinetic energy cutoff of 200 Ry and 216 \mathbf{k} points. Cases requiring a fully-relativistic treatment are computed at a reduced setup of $4\times 4\times 4$ \mathbf{k} points, $2\times 2\times 2$ \mathbf{q} , and a kinetic energy cutoff of 100 Ry. This setup does not show deviations in the band structures from the higher setup for exemplary test cases. The band structure interpolation is performed with WANNIER90 using all bands.²⁷ In all band structure plots, high-symmetry points are denoted according to the AFLOWLIB standard (TRI_{1b}).²⁸ The polarization is also obtained for the optimized PBE geometry. It was obtained within the Berry phase formalism, as implemented in QUANTUMESPRESSO. A grid of 6×6 strings with seven points along the evaluated direction gives converged results.

Results and Discussion

Traditionally, the Goldschmidt tolerance factor²⁹ is used as indication for the preference of ABX_3 compositions to crystallize as perovskite. This concept has also been extended to organic molecules in HP.³⁰ We can further extend this concept for IPs and IHPs. However, we must keep in mind that anionic radii are less established for many metals than cationic radii and that the tolerance factor is only an indicator,³¹ with acceptable values ranging typically from $t = 0.75 - 1.0$. We adopt this strategy by using tabulated ionic radii. Whenever specific ionic states are not reported in the seminal works of Shannon,^{32,33} we evaluated new ionic radii by harvesting the data available in the Materials Project.³⁴ In short, we adopt Shannon's initial assumptions that i) ionic bonds can be decomposed into radii of their constituent ions to a sufficient degree of accuracy and ii) the ionic radii of species are directly dependent on their oxidation state and coordination number. By harvesting binary alkali and alkaline-earth metal compounds, we determine the ionic radius of a desired element, depending on the required oxidation state and coordination number. For cases where the radius of a desired coordination number to a given oxidation state is still unknown, we obtain it from linear interpolation. For now, we only obtain new values by this procedure, i.e., whenever the obtained data would change one of the established ionic radii from Shannon, we apply a shift to the linear function between CN and $r_{\text{ionic}}(\text{CN})$ in order to retain the old value. Details of this, together with our implementation, will be published elsewhere.³⁵

In order to design IHPs, we first realize that common X -site anions in perovskites have ionic radii of 1.26 Å to 2.06 Å (ionic radii between O^{2-} and I^-). Thus, in order to be able to build perovskites with inorganic anions (another possibility would be double hybrids,¹⁴ which we will not investigate here), we have to choose a small cation within this range for the X -site. Furthermore, the chosen molecule must be able to serve as a bidentate bridging ligand in order to be suitable for the X -site. An organic cation that may serve as bridging ligand, CH_3NH_3^+ (MA), is small (estimated effective ionic radius of about 2.17 Å, for a discussion see the supporting information of Gebhardt et al.¹)³⁰ and is currently under the limelight of

hybrid-perovskite research.

After choosing monovalent MA for the X -site, we seek mono- and divalent anions to form MA_3BA structures. The site preference of these anions is not initially clear: On one hand, a^{2-} ions should generally be larger than a^- anions and favor the A -site, although the effect of oxidation state on ionic radii of anions is less pronounced than for cations. On the other hand, the B -site provides a closer proximity to the cations, which should be favorable for the anion in the higher oxidation state due to the greater Coulombic attraction. Thus, in contrast to conventional perovskites where these effects go hand in hand, they are competing in the case of IPs. Overall, the site preference will be dominated by the composition of ionic radii and the relative size differences. However, this might facilitate the interchange of mono- and divalent anions between A - and B -sites and will require testing the preference of A - vs. B - site occupation in cases where the difference between anionic radii is small.

Chalcogenide Halides

Natural choices for mono- and divalent anions are halides and chalcogenides, respectively, and we start our search for suitable $(\text{MA})_3\text{BA}$ compounds with these elements. We begin by choosing $A=\text{I}^-$ and searching for suitable B^{2-} anions. All $(\text{MA})_3\text{BI}$ compounds with $B=\text{O}$, S, Se, Te have tolerance factors of 0.71 – 0.90 and could, therefore, form stable IHPs, with Te and Se compounds being on the fringe where other structures become more likely.²⁹ We find that O and S are protonated (H_2O and HS^- , see below), leading to interesting structures. The resulting hydrogen bonded network differs from traditional HPs or other IHPs below, since protonation on the B -site reduces the ionic character. For O, the structure is shown in Fig. 1 (a-c), and the structural properties are summarized in Table 1. In general, MA units on the X -sites are tilted, allowing every molecule to bridge two B -site oxygens *via* hydrogen bonds to the CH_3 and the NH_3 groups, respectively, in a head-on $B \cdots \text{NH}_3 - \text{CH}_3 \cdots B$ motif. Three MA units are oriented head-on with their NH_3 groups towards the B -site center, each sharing one of the acidic N–H hydrogen atoms with the central atom.

For $B=O$, two of these N–H bonds are significantly larger (about 0.6 Å) than the O–H bond; i.e., a water molecule is formed in the center of the BX_6 octahedron and the formula unit reads as $(CH_3NH_3^+)(CH_3NH_2)_2(H_2O)I^-$. In this compound, BX interactions are dominated by hydrogen bonds between the protonated B -site and the surrounding MA cations and molecules. Two hydrogen bonds are formed between water hydrogens and lone-pairs of the resulting NH_2 groups, and a third hydrogen bond forms between one lone-pair of O and the acidic proton of the remaining MA cation. Such a motif suggests temperature-dependent dynamical proton exchange between the B -site oxygen and the surrounding MA cations. The remaining three corners of the BX_6 octahedron are occupied with CH_3 groups, each pointing with one H atom towards the O center. This means that the second lone-pair of each O atom has three additional H atoms from CH_3 groups within the typical range for hydrogen bonding (2.5 Å).

The band structure and DoS of $(CH_3NH_3^+)(CH_3NH_2)_2(H_2O)I^-$ are displayed in Fig. 2 (a-b), showing a wide band-gap semiconductor with an indirect band gap of 4.69 eV at the PBE level. Comparison to more accurate HSE calculations (see Table 1) suggests that the true band gap is underestimated by ≈ 1.31 eV. As noted before,¹ the expected inversion of band character is found when comparing IHPs to HPs, i.e., we observe dominant contributions of B - and A -site anions at the valence band (VB) edge and from the X -site cation at the conduction band (CB) edge. However, whereas A - and B -site energies are well separated in most traditional perovskites, with the latter dominating the VBs, we observe contributions from both anions close to the Fermi level in $(MA)_3OI$. This indicates that states attributed to the B -site are stabilized with respect to states attributed to the A -site anion. We can understand this by a stabilization of Op bands due to the covalent bond formation in the water molecule in comparison to the ionic bonding that fills the I valence p shell. In addition, some Np character mixes with I bands at the VBE. These contributions can be attributed to the N atoms of the deprotonated CH_3NH_2 molecules.

In order to investigate the stability of these new IHP materials, we selected $(MA)_3FPb$

Table 1: Tolerance factor t , structure information, formation energies E_{form} , and band gap E_g for the investigated $(\text{MA})_3\text{BA}$ compounds. For cases with indirect band gap, the direct band gap E_g^{dir} is given in parentheses. Boldface values were computed using hybrid-DFT. For the stable, non-metallic composites the polarization \mathbf{P} is given. \mathbf{P} =perovskite, \mathbf{P}_{\perp} =side-on structure, ' =distorted structure

System	t	Structure	$V/\text{atom}/\text{\AA}^3$	$a_0/\text{\AA}$	$b_0/\text{\AA}$	$c_0/\text{\AA}$	α	β	γ	$E_g(E_g^{\text{dir}})/E_g^{\text{fcl}}(E_g^{\text{fcl,dir}})/\text{eV}$	$E_{\text{form}}/\text{eV/f.u.}$	$\mathbf{P}/(\mu\text{C}/\text{cm}^2)$
$(\text{MA})_3\text{OI}$	0.90	P	9.23	5.95	6.56	6.16	92.08	93.39	91.35	4.69 (4.80), 5.90	-0.16	38.0
$(\text{MA})_3\text{SI}$	0.79	\mathbf{P}_{\perp}	10.40	6.19	7.45	5.97	84.17	86.58	81.52	4.14 (4.18), 5.32	0.33	57.0
$(\text{MA})_3\text{SeI}$	0.76	CaIrO_3	9.18	7.03	6.93	5.23	94.75	71.89	99.88	3.18 (3.39), 4.16	0.57	57.6
$(\text{MA})_3\text{TeI}$	0.71	CaIrO_3	9.36	7.15	6.94	5.28	94.25	69.68	97.76	3.22 (3.34)	0.23	52.4
$(\text{MA})_3\text{TeBr}$	0.68	CaIrO_3	9.05	7.12	6.79	5.28	96.11	68.66	97.89	3.36 (3.45)	0.11	55.2
$(\text{MA})_3\text{TeCl}$	0.65	CaIrO_3	9.00	7.13	6.75	5.28	96.88	68.70	97.96	3.56 (3.64)	0.12	56.7
$(\text{MA})_3\text{TeF}$	0.58	CaIrO_3	8.62	7.14	6.36	5.33	97.56	70.81	100.23	3.56 (3.75)	0.14	—
$(\text{MA})_3\text{ITe}$	0.69	CaIrO_3	9.30	7.16	6.88	5.28	93.14	69.68	97.21	2.43 (2.61)	0.74	—
$(\text{MA})_3\text{BrTe}$	0.76	\mathbf{P}_{\perp}	9.09	6.18	6.47	5.91	89.51	89.29	90.35	2.90 (3.07)	0.58	—
$(\text{MA})_3\text{ClTe}$	0.79	\mathbf{P}_{\perp}	8.85	6.10	6.32	5.97	90.87	90.88	89.51	2.94 (3.21)	0.45	—
$(\text{MA})_3\text{FTe}$	0.90	P	8.84	6.00	6.46	5.93	91.28	90.28	89.79	2.99 (3.38), 3.89	-0.22	44.2
$(\text{MA})_3\text{FS}$	0.80	P	7.62	5.67	6.35	5.51	91.16	89.36	89.52	3.40(3.68), 4.42	0.49	41.4
$(\text{MA})_3\text{FSe}$	0.85	P	7.84	5.74	6.32	5.63	91.33	89.97	89.71	3.17(3.53), 4.09	0.35	41.0
$(\text{MA})_3\text{GaI}$	0.74	$A-B(\text{GaH}_2\text{I})$	8.80	6.72	5.12	7.35	107.67	80.07	107.14	metallic	-1.63	—
$(\text{MA})_3\text{FGa}$	0.91	P	8.11	5.66	6.39	5.86	94.08	92.36	92.44	metallic/metallic	1.39	—
$(\text{MA})_3\text{TII}$	0.71	CaIrO_3	9.37	7.21	7.02	5.11	93.08	70.69	93.72	metallic/metallic	1.71	—
$(\text{MA})_3\text{ITl}$	0.75	CaIrO_3	9.53	7.24	7.03	5.17	93.51	71.10	95.35	metallic/metallic	1.75	—
$(\text{MA})_3\text{FTl}$	0.94	P	8.65	5.84	6.48	5.95	92.77	91.51	91.23	metallic/metallic	1.32	—
$(\text{MA})_3\text{TIF}$	0.57	CaIrO_3	8.62	7.37	6.48	5.07	101.20	71.10	97.84	metallic/metallic	1.53	—
$(\text{MA})_3\text{GeI}$	0.74	$A-B(\text{GeH}_2\text{I})$	9.33	6.89	5.40	7.07	107.64	81.30	103.63	3.04(3.09)	-0.27	—
$(\text{MA})_3\text{FGe}$	0.91	P	8.02	5.67	6.35	5.80	92.79	90.92	91.16	metallic/metallic	2.48	—
$(\text{MA})_3\text{FSn}$	0.96	P	8.44	5.77	6.43	5.92	92.09	90.86	90.76	metallic/metallic	1.05	—
$(\text{MA})_3\text{IPb}$	0.77	CaIrO_3'	9.51	6.04	6.54	7.12	75.34	104.32	113.08	0.13(0.31)/0.25(0.33), 0.74/0.76	0.83	—
$(\text{MA})_3\text{FPb}$	0.96	P	8.63	5.86	6.45	5.94	91.76	90.76	90.38	metallic/metallic	0.91	19.1
$(\text{MA})_3\text{SeTl}$	0.75	$A-B(\text{SeTl})$	8.69	6.54	6.82	5.34	89.83	85.54	72.10	0.24(0.61)/0.29(0.61)	1.44	—
$(\text{MA})_3\text{SeBi}$	0.77	\mathbf{P}_{\perp}	8.76	6.22	6.62	6.00	76.85	71.82	90.14	1.37(1.50)/1.24(1.38), 2.17/1.94	0.99	—
$(\text{MA})_3\text{NaTe}$	—	$A-B(\text{NaTe})$	8.09	6.24	5.31	6.78	82.46	108.58	96.03	—	-2.73	—
$(\text{MA})_3\text{SeRb}$	—	P	10.73	5.98	7.35	6.43	98.49	89.15	92.80	0.48(0.62)	1.82	—

as an example and computed the phonon band structure. No indications of instability in the form of unstable phonons were found for this material (see Gebhardt et al.¹ and its supporting information). To assess stability toward decomposition, we compute the formation energy for the reaction $(\text{MA})_2a^{2-} + \text{MA}a^- \rightarrow (\text{MA})_3a^{2-}a^-$, which serves as standard route in HP synthesis (see below for details). $(\text{MA})_3\text{OI}$ is thermodynamically stable with respect to the investigated decomposition path by -0.16eV per formula unit (f.u.). We also tried to employ a different organic cation, namely dimethylammonium $\text{CH}_3\text{NH}_2^+\text{CH}_3$ (DMA). The latter is symmetric, with two CH_3 groups that could serve as possible anchor groups for B -H bonding. The methyl H atoms are much less acidic and could suppress B -site protonation. However, we find that the attraction of O and H dominates, leading to a rotation of the DMA molecules to enable formation of water by abstracting the acidic proton from the central NH_2^+ group. Such a rearrangement does not permit the perovskite structure, and we

leave this kind of modification to future studies. Instead, we examine heavier chalcogens, i.e., elements that less strongly attract hydrogen.

(MA)₃SI behaves similarly to (MA)₃OI; however, in line with the reduced electronegativity of S compared to O, *B*-site S only binds one proton, forming HS⁻ anions [(CH₃NH₃⁺)₂(CH₃NH₂)(HS⁻)I, see Fig. 1 (d-f)]. Unlike the oxygen case, the S–H bond is not oriented toward MA units and, hence, does not contribute to the hydrogen bonding. Instead, the deprotonated CH₃NH₂ molecule is oriented toward one of the intact MA cations, forming a hydrogen bond between the acidic hydrogen of the NH₃ group and the lone-pair of the NH₂ group. The electronic structure of (MA)₃SI (Fig. 2 (c, d)) is similar to the oxide case. However, due to bonding to only one H atom, the stabilization of S states is less pronounced compared to the O case, and the S *B*-site bands are slightly above the *A*-site I bands. The PBE band gap of (MA)₃SI is 4.14 eV, which is only marginally smaller (0.04 eV) than the smallest direct gap. The band gap of (MA)₃SI is 0.55 eV lower than that of (MA)₃OI at the PBE level, nearly the same as at the HSE level (0.58 eV). This suggests that relative trends are well described at the GGA level, as it has been observed for many other materials.

As reported earlier,¹ by considering heavier, less electronegative chalcogenides, protonation is successfully suppressed, i.e., (MA)₃SeI and (MA)₃TeI remain intact. However, we find that a different structure (Fig. 1 (i, j)), with both corner- and edge-sharing octahedra (CaIrO₃ structure), is energetically preferred by 0.32 and 0.72 eV/f.u. compared to the perovskite structure for the Se and Te compound, respectively. In this structure, *B* ⋯ *X* ⋯ *B* bridging involves only the NH₃ head of MA units in one plane and an *X*-site double layer separates neighboring *B*-sites along the third direction. The electronic structure of (MA)₃SeI is shown in Fig. 2 (e, f). Despite the phase change, the electronic structures look similar, and the Se case appears truly inverted in the sense that the filled *B*-site anion bands are located above the *A*-site bands. In addition, the N contribution at the VB edge is much less pronounced, in line with the cationic character of all MA units. Besides the stronger ionic character, the formation energy of (MA)₃SeI is less favorable compared to the oxygen

and sulfur analogs. This demonstrates the stability of the hydrogen bonded perovskites, and indicates a penalty due to an increasingly worse tolerance factor for heavier chalcogens and the resulting phase change.

The ionic radii of Te^{2-} and I^- are almost identical. On one hand, this means that a structural alternative to the IHP becomes more likely. On the other hand, this means that the site preference of the two anions is ambiguous and cannot be determined based on ionic radii. We, therefore, compare $(\text{MA})_3\text{TeI}$ and $(\text{MA})_3\text{ITe}$ in different structures, finding that $(\text{MA})_3\text{TeI}$ in the CaIrO_3 structure is the thermodynamic minimum, being 0.51 eV more stable than the CaIrO_3 structure with exchanged anion positions and 0.72 eV more stable than the perovskite structure (Fig. 3). These results are in line with our hypothesis that the divalent anion prefers the B -site whenever the two anions are of similar size, because of a stronger interaction with the X -site cations. The perovskite structures for this composition differ from the previous cases (Fig. 1 (k, l)). The MA units are not tilted and oriented perpendicular to the $B \cdots X \cdots B$ axis. As a result, the bridging motif changes as the two heads of each MA cation interact simultaneously with both B -sites. This structural change allows a larger B -site anion and is frequently found for cases with $t < 0.80$, i.e., the tilt angle of the MA X -site cations adopts to the structural fit of the X_3BA composition. We introduce the label P_\perp to indicate cases where hydrogen bonds of B sites to the CH_3 and NH_3 heads of MA units are both in a similar range smaller than 3 Å. Despite this structural flexibility in the IHP structure, systems with small tolerance factors (here $t \approx 0.70$) favor the CaIrO_3 over the perovskite phase energetically.

Therefore, we try to stabilize the perovskite phase by altering the halide (Fig. 3). $(\text{MA})_3\text{BrTe}$ and $(\text{MA})_3\text{ClTe}$ have improved tolerance factors of $t = 0.76$ and $t = 0.79$, respectively. Consequently, these compounds do prefer the perovskite structure. However, we find that these compositions are further stabilized by interchanging anion positions. Since these structures with B -site Te^{2-} have very small t values ($\text{Br}=0.68$, $\text{Cl}=0.65$), they favor the CaIrO_3 phase. With $t = 0.9$, $(\text{MA})_3\text{FTe}$ favors the perovskite structure and is significantly stabi-

lized compared to $(\text{MA})_3\text{TeF}$. In agreement with the larger tolerance factor, we observe a highly ordered IHP structure with tilted MA units and head-on $B \cdots X \cdots B$ bridging motif (Fig. 1 (g, h)). This demonstrates that the site preference of mono- and divalent anions can indeed be changed by tuning t . Based on this insight, we are able to successfully form chalcogenide halides in the perovskite structure for all chalcogenides. In addition to $(\text{MA})_3\text{OI}$ and $(\text{MA})_3\text{SI}$, the fluorides $(\text{MA})_3\text{FS}$, $(\text{MA})_3\text{FSe}$, and $(\text{MA})_3\text{FTe}$ all prefer to form perovskites. These compounds are either thermodynamically stable or show only a small tendency toward decomposition ($E_{\text{form}} \leq 0.49 \text{ eV/f.u.}$), suggesting that these novel compounds should be accessible. Others, such as $(\text{MA})_3\text{BrTe}$ or $(\text{MA})_3\text{ClTe}$ may be accessible via ion-exchange synthesis.³⁶

All investigated chalcogenide halides are wide band-gap semiconductors. As such, they could be interesting for superionic conduction or proton conduction, as it is observed in inorganic IP.^{10,11} The band gap is tunable via both B - and A -site anion substitution. For the same composition, perovskite compounds have smaller band gaps than CaIrO_3 phases. When adjusting the composition of tellurides, the band gap is reduced by increasing the size of the halogen atom. Similarly, the band gap is also decreased by employing heavier chalcogenides. Overall, the DFT band gaps are tunable in the range of 2.43 eV to 4.69 eV. For the investigated chalcogenide halides, PBE band gaps are underestimated by $E_g^{\text{HSE}} - E_g^{\text{PBE}} \approx 1.04 \pm 0.13 \text{ eV}$.

As we have shown for $(\text{MA})_3\text{FTe}$,¹ IHPs show pronounced off-center displacements that arise from lattice distortions from the cubic phase as well as natural displacements due to uneven hydrogen bonding of B -site anions to CH_3 and NH_3 units. As shown in Table 1, this gives rise to large polarization for all compounds, with values of the order of prototypical ferroelectric materials like BaTiO_3 . Hence, once these new materials are successfully synthesized, they should be tested for their ferroelectric properties.

Next we analyze the influence of the chosen unit cell size. To do so we also computed a $(2 \times 2 \times 2)$ cell of $(\text{MA})_3\text{FTe}$. We do not find any energetic stabilization by increasing the

cell size. Consequently, structural changes, e.g., octahedral tilting, are not observed in this material. Since this is a material with tolerance factor close to 1, we repeat this test for a composition that should show larger tendency for deformation, $(\text{MA})_3\text{ITe}$ ($t = 0.69$). Again, we do observe neither energetic stabilization nor noticeable structural changes like octahedral rotations when considering the larger cell. This can be explained by the observed reduced tilting of MA units in the P_\perp structure. IHPs adopt their structure for $t < 1$ by tilting the MA units on the $B \cdots X \cdots B$ axis. Based on our results, this is preferred over alternative structural relaxations such as octahedral rotations. This is complementary to most (hybrid) perovskite materials, since such a process is not possible with spherical X -site ions. It suggests an easier design of IHP composition that allows larger deviations in t . On the other hand, the sensitivity of the tilting angle of the bridging ligand on t could be useful to spot defects or dopants in IHPs. Furthermore, this demonstrates that the orientation of organic ligands in any hybrid perovskite is important and should be taken into account when evaluating t in the future.

For the remaining chalcogenide halides, we can now evaluate tolerance factors, in order to identify promising compounds. The results are summarized in Fig. 4. Our extensive tests for the chalcogenide halides allow to establish a threshold tolerance factor of $t \approx 0.76$. Structures with larger t can be expected to form stable perovskites, whereas compounds with smaller t are likely to be either unstable or to form a different phase, e.g., CaIrO_3 . For tolerance factors around this threshold, a small intermediate region exists where compounds can prefer the perovskite $((\text{MA})_3\text{BrTe})$ or a distorted CaIrO_3 phase $((\text{MA})_3\text{IPb})$. Divalent anions on the B -site are problematic for two reasons: firstly, they tend to be protonated, reducing the ionic bonding character; secondly, they are usually too large for successful pairing with A -site halides. For the chalcogenide iodides, only $(\text{MA})_3\text{OI}$ has a good tolerance factor, with $(\text{MA})_3\text{SI}$ already being close to the threshold value where other phases become favorable. All other compositions favor the CaIrO_3 phase and only improve t when the anionic sites are interchanged. Consequently, the most promising compounds employ B -site fluoride.

Although some bromide and chloride compounds also have promising t , fluoride is always favorable. However, other halides can be considered for tuning the electronic structure.

The results obtained for chalcogenide halides can now guide our search for appropriate compositions including elements from other groups of the periodic system (Fig. 4). As mentioned above, we want to explore other main group elements for their ability to form mono- or divalent ions by partly filling their valence shells. Few alkali metals compounds are known where the alkali metal fills its valence s -shell (alkalides),³⁷ forming a monovalent anion. Although unlikely, we explore this possibility by considering $a^- = \text{Na}$ and Rb (note that we did not compute tolerance factors for alkalides, since ionic radii for these special cases are unknown and cannot be obtained by our method).³⁵ Alkaline-earth metals are not known in anionic oxidation states. Groups XIII through XV can, in principle, add electrons to their valence p shell. Although they prefer a complete filling of their valence shell, fractional filling is possible. Since light chalcogenides showed a tendency for protonation on the B -site, we will focus on heavier elements of the fourth row and below (Ga , Tl , Ge , Sn , Pb , and Bi).

Other divalent anions

Naively, icosagens could form high-spin divalent ions by occupying one spin-component of their valence p shell. Based on our estimated ionic radii, gallium, indium, and thallium 2- are about the size of Te^{2-} . Consequently, iodides have tolerance factors below the perovskite threshold, and we do not observe any stable perovskite. In the case of $(\text{MA})_3\text{GaI}$ we observe again protonation of the B -site anion, forming GaH_2 . As a result, only one MA cation remains intact, whereas the other two orient their NH_2 groups with the nitrogen lone-pair toward one of the hydrogen atoms of the MA cation, forming hydrogen bonds. Furthermore, Ga is bonded to one I in a distance of 2.75 \AA , which is in line with Ga-I bonds in, e.g., GaI_3 ,³⁸ suggesting covalent interaction between these two groups and the formation of a GaH_2I^- unit to address the electron deficit at the gallium center. In fact, similar trihalogen icosagen compounds are known to combine to $X_3\text{Ga-GaX}_3^{2-}$ units.³⁹ Such an icosagen-

icosagen bond is not possible in the chosen unit cell. Instead, we observe the formation of a zig-zag chain of GaH_2I^- units with a second Ga–I distance that is elongated by only 0.05 Å. Such a bonding motif of chains connecting *A* and *B* site ions occasionally occurs for light divalent anions on the *B*-site. We denote it *A-B* here, adding the coordination of the *B*-site in brackets (Table 1). Albeit this bonding motif is of intellectual interest with respect to gallium chemistry, these results indicate that such compositions are unsuited to form IHPs. Furthermore, the resulting structures could be unstable compared to other phases and we keep these cases solely for completeness without analyzing the electronic structure in detail.

Since protonation at the *B*-site was successfully prevented by employing heavy chalcogens above, we also study thallium compounds. Despite an ionic radii of Tl^{2-} that is estimated to be slightly larger compared to I^- , thallium energetically favors the *B*-site in conjunction with iodide. In line with a small tolerance factor ($t = 0.71$), we find that $(\text{MA})_3\text{TlI}$ favors the CaIrO_3 phase. In this structure, the thallium *B*-site preference is small (0.04 eV). The stabilization over the perovskite structure is 0.33 eV and 0.19 eV per f.u. for thallium on the *B*- and *A*-site, respectively, i.e., less pronounced than in the tellurium-iodide compounds.

For heavy elements like Tl, we investigate the influence of SOC. $(\text{MA})_3\text{TlI}$ is metallic with or without SOC, i.e., the consequences of SOC on the band structure are small (Fig. 5 (c, d)). Nevertheless, we find the same Dirac-cone like crossings at all high-symmetry points as reported¹ for $(\text{MA})_3\text{FPb}$, due to the splitting of the valence *p* bands. We find that the two valence $\text{Tlp } j = 1/2$ bands are filled, whereas the lower pair of $j = 3/2$ is fractionally filled. This suggests that Tl is indeed in oxidation state 2-. Metallic IHPs like this could share interesting properties like giant magnetoresistance,⁴ superconductivity,² or negative thermal expansion³ with their inorganic counterpart.⁴⁰

Similar to the larger chalcogens, a site change and stabilization of the perovskite structure can be induced by substituting iodide by fluoride. For $(\text{MA})_3\text{FTl}$, we obtain a well-ordered perovskite. The Tlp bands (Fig. 5 (a, b)) are again located around the Fermi level. In comparison to the *A*-site I bands, *B*-site F bands are stabilized by about 2 eV. In case of

(MA)₃FGa, the valence p bands remain pair-wise degenerate, due to the smaller SOC in the lighter element (not shown). Otherwise, the electronic structure is mostly unchanged and dominated by the valence p bands. The distance to the lower-lying occupied bands is in both cases roughly 5 eV. However, for Ga the 4s shell is slightly lifted toward higher energies than the B -site F bands (not shown), whereas fluoride and Tl 6s show hybridization.

In any case, the group XIII elements prefer a low-spin filling of their valence p shells, resulting in the discussed fractional filling of the lower pair of $j = 3/2$ bands. Despite the fractionally-filled valence shell, (MA)₃FTl remains nonmagnetic in the primitive unit cell. Also in a larger (2×2×2) structure, no stable magnetic configuration is found. However, an antiferromagnetic configuration leads to a stabilization of −0.19 eV. This stabilization improves the formation energy (0.94 eV) compared to the primitive cell, but it remains thermodynamically unstable. Even in this case, the magnetic moment of the Tl atoms is small, i.e., we can safely exclude any high-spin magnetic structure. Overall, compounds containing divalent anions of group XIII elements are metallic and have high formation energies and, therefore, are unsuitable for IHPs.

Next, we can try to obtain semiconducting systems by two approaches: (i) remove one electron from the system by employing group XIII elements as monovalent ion (see below) or (ii) add another electron by employing group XIV elements instead. Moving toward group XIV, we observe very similar results comparing, Ge and Ga. Germanium is again protonated, and an A - B structure with GeH₂I is formed (Ge-I distance of 2.74 Å, similar to the discussed gallium case and in line with Ge-I bonds, as found in conventional germanium-iodine perovskites).⁴¹ Due to the additional electron compared to group XIII elements, GeH₂I does not form a chain, but has a lone-pair on the germanium atom instead. We again try to suppress this protonation by considering a heavier element. (MA)₃IPb shows indeed no Pb-H bonds, but due to the tolerance factor of 0.72, the CaIrO₃ phase is thermodynamically favorable. The most stable structure deviates from the ideal CaIrO₃ structure by the position of two MA units, leading to a different connectivity of the edge-sharing BX_2 planes. This

structure is 0.80 and 0.97 eV per f.u. more stable than the perovskite or the CaIrO_3 structure and suggests that a completely different phase could be more stable. Of course, compositions with low tolerance factors will also be in competition with other stoichiometries, e.g., for this case the well-known MAPbI_3 . Nevertheless, we investigate the electronic structure in Fig. 6 (a). Compared to $(\text{MA})_3\text{FTl}$, the extra electron leads to the emergence of a small band gap between the two pairs of SOC-split $j = 3/2$ bands. This is an interesting electronic structure with relatively small band gap of 0.74 eV at the HSE level. The linear crossings at high-symmetry points in the valence p bands are observed, analogously to the Tl case.

Again, we expect the stabilization of the IHP structure when improving the tolerance factor by using a smaller B -site halogen. Therefore, we also compute the properties of $(\text{MA})_3\text{FPb}$ in the perovskite structure, and the electronic structure is shown in Fig. 6 (b,c). The Fermi level is again located in between the $j = 3/2$ bands. However, in some regions of the BZ we observe a fractional occupation of both sets, i.e., $(\text{MA})_3\text{FPb}$ is overall metallic and not a small band-gap semiconductor such as $(\text{MA})_3\text{IPb}$.

Very similar behavior is also observed for $(\text{MA})_3\text{FSn}$ (Fig. 6 (d)), i.e., a metallic band structure, with interesting linear band crossings around the Fermi level. A metallic band structure is also found for $(\text{MA})_3\text{FGe}$, however, due to reduced SOC no noticeable splitting of the $j = 3/2$ bands is shown, i.e., the latter remain twofold degenerate (not shown).

Other monovalent anions

Similar strategies as above can also be explored to find other monovalent anions. Group XIV ions could form a^{-1} ions by forming a half-filled valence p shell. However, as before we observe that such a high-spin structure is unstable. Consequently, $(\text{MA})_3\text{GeTe}$ forms similar zig-zag chains as found in $(\text{MA})_3\text{GeI}$ and $(\text{MA})_3\text{GaI}$. Instead, we can try to fill the $j = 1/2$ bands by employing a group XIII element. In order to prevent B -site protonation, we know from the results above that we have to choose heavy elements. $(\text{MA})_3\text{SeTl}$ has with $t = 0.75$ the most promising tolerance factor. However, this t is still quite small and below our threshold

for IHPs. Consequently, we do not observe a perovskite, but the formation of Se–Tl bonds in an A – B structure. The electronic structure (Fig. 7 (a, b)) reveals a filling of all Se p and one Tl p band, suggesting the correct oxidation states of 2- and 1-. Furthermore, the PBE band gap of 0.29 eV is expected to be perfectly suited for photovoltaic applications, since IHP gaps are underestimated by about 1.04 eV. Unfortunately, the unfavorable formation energy and the described structural changes indicate that other phases are more important for this composition. To improve t and to stabilize the IHP structure, compositions employing smaller chalcogenides (accompanied by B -site protonation) can be considered in the future.

Next, we try Bi as monovalent anion in order to fill the lower pair of $j = 3/2$ bands similar to (MA)₃FPb. The estimated tolerance factor ($t = 0.77$) is close to our threshold value. In our structural search we find that the perovskite structure is favorable, albeit it is distorted and shows untilted MA units in a P_{\perp} arrangement. The electronic structure (Fig. 7 (c, d)) indeed shows the expected band gap within the Bi valence p bands. With 1.94 eV at the HSE level including SOC, it is at the upper limit for photovoltaic applications. The DoS shows strong Se and Bi p band mixing, in line with the observed structural changes. However, as a lead-free alternative,^{42,43} replacing Pb by other heavy metals (Tl and Bi) is, if any (Tl),⁴⁴ only a slight improvement. Therefore, from a toxicity stand point, other alternatives must be found to improve on the lead-halide photovoltaics. One possible route is the inclusion of transition metals.

As final possibility, we consider the formation of B - and A -site alkalides in the compounds (MA)₃NaTe and (MA)₃SeRb, respectively. Alkali metals are unsuitable on the B -site. (MA)₃NaTe favors an A – B structure accompanied by H₂ formation over the perovskite or CaIrO₃ structures. On the A -site, (MA)₃SeRb favors the P_{\perp} structure. The electronic structure (not shown) differs significantly from all other cases. It reveals that the Rb valence s shell is empty, with the highest occupied band being the $4p$ shell. This means that Rb remains in its common oxidation state, +1. Consequently, two of the MA molecules are neutral, leading to a band gap between MA states of 0.53 eV at the PBE level. In summary,

the formation of alkalides is not successful. This is not surprising, since the latter require specialized ligands such as cryptands to be stabilized.

$\text{MA}a^-$ and $(\text{MA})_2a^{2-}$ reference structures

In the following, we describe the results obtained for the reference compounds of mono- and divalent anions $\text{MA}a^-$ and $(\text{MA})_2a^{2-}$. $\text{MA}a^-$ halide compounds have been studied previously, showing a variety of phase transitions.⁴⁵ Not all phases have been characterized successfully; however, one crystal structure has been reported for each case, namely an orthorhombic structure in space group 57 for MAI (low-temperature δ phase),⁴⁵ a tetragonal structure in space group 129 for MABr (room-temperature α phase),⁴⁶ a similar tetragonal structure with the same symmetry but with a simpler stacking motif for MACl (α'),⁴⁷ and a trigonal structure in space group 160 for MAF⁴⁸ (this is a low-temperature structure (123 K), that we call β phase). Besides the δ phase found at low temperatures for MAI, MABr, and MACl, there exists another low-temperature phase. This β phase has, however, not been characterized yet. Due to the size difference of fluoride and the other halides, it is possible that they have different β phases, i.e., a reliable model for the β phases of MAI, MABr, and MACl is unknown at present. Nevertheless, our evaluation in Table 2 shows that all phases, except the MAF β phase for I and Br, are close in energy. This means that the potential energy surface of these compounds is rather flat, in line with many local minima due to different orientations of the organic molecules. Due to small energy differences, any phase should provide a useful reference for our purpose. The only case that differs is MAF. Due to the small fluoride ions, adjacent MA ions are too close in the δ phase, which is indicated by an observed tilting of these ions. Compared to that, both α phases are stabilized by about -0.16 eV. The thermodynamic minimum is the reported β phase. This phase clearly favors small anions, as shown by the increasing destabilization in the halide group.

The experimentally available structural information is compared with our calculated results in Table 3. Our setup shows a systematic overbinding with slightly too small lattice

Table 2: Phase stabilities for $\text{MA}a^-$ reference compounds relative to the δ phase. For the calculated formation energies we use the thermodynamic minimum for each compound.

Compound	$E(\alpha) - E(\delta)/\text{eV}$	$E(\alpha') - E(\delta)/\text{eV}$	$E(\beta) - E(\delta)/\text{eV}$
MAI	0.02	-0.01	1.69
MABr	0.02	0.01	0.75
MACl	-0.04	0.00	0.14
MAF	-0.17	-0.16	-0.23

constants. However, the computed results are overall in reasonable agreement with the experimental results. Hence, our structural data for IHPs should have good predictive power for future experiments.

Table 3: Comparison of experimental and computed $\text{MA}a^-$ structures.

Compound(Phase)	$a_0/\text{\AA}$	$b_0/\text{\AA}$	$c_0/\text{\AA}$	Ref.
MAI(δ)	7.17	7.10	8.83	Exp. ⁴⁵
	7.03	6.93	8.61	PBE+D2
MABr(α)	4.81	4.81	8.74	Exp. ⁴⁶
	4.68	4.64	8.31	PBE+D2
MACl(α')	6.04	6.04	5.05	Exp. ⁴⁷
	5.95	5.96	4.74	PBE+D2
MAF(β)	4.43	4.43	13.53	Exp. ⁴⁸
	4.33	4.33	12.97	PBE+D2

In contrast, $(\text{MA})_2a^{2-}$ compounds have not been studied in the past. A survey of alkali and alkaline-earth metal chalcogenide compounds reveals that most of them crystallize in the CaF_2 structure. We take this as starting point, replacing the metal cation with MA. For $(\text{MA})_2\text{Se}$ we find that an alternating arrangement of MA units along all spatial directions in a crossed configuration is energetically favorable, and we use this structure as starting point for the other compounds. During our studies, we observe that the S, Se, Te, Sn, and Pb compounds prefer a trigonal phase (space group 164). This phase results from a reorientation of the MA molecules to a parallel arrangement (Fig. 8 (c, d)). Ga, Tl, and Ge favor an arrangement of MA molecules that is in between the other two phases, resulting in a distorted low-symmetry phase (space group 2, Fig. 8 (e, f)). Thus, only $(\text{MA})_2\text{O}$, where the

formation of water molecules is observed, favors a structure that is related to CaF_2 (Fig. 8 (a, b)). The formation of water in $(\text{CH}_3\text{NH}_2)_2\text{H}_2\text{O}$ appears to stabilize this structure, whereas less electronegative anions tend to favor the trigonal phase.

Conclusion

We present an extensive materials search for a recently proposed novel materials class (IHP). Searching for mono- and divalent ion compositions, we demonstrate the ability and limitations of chalcogenide halides to form IHPs. IHPs are structurally flexible. Different tilting of MA units along the $B \cdots X \cdots B$ axis leads to different bonding motifs and balances deviations from an ideal tolerance factor, suppressing the need of octahedral rotations. A threshold tolerance factor of $t > 0.76$ is established. Compositions with smaller t favor the related CaIrO_3 structure. Consequently, only the smallest chalcogenides (O^{2-} and S^{2-}) are suitable B -site anions. These electronegative anions are protonated. This leads to a reduction of the ionic character of the hydrogen bonded BX_6 octahedra and indicates dynamical proton transfers within octahedra. The general inequality of bonding sites in MA as bridging ligand leads to large polarization, indicating a natural use of IHPs for piezoelectric or ferroelectric applications. Heavier, less electronegative chalcogenides can be employed by swapping the anionic sites. Best suited are $(\text{MA})_3\text{FA}$ compounds. Electronically, chalcogenide halide IHPs have large band gaps. Changing the anion composition allows for a variable tuning of the band gap from wide band-gap semiconductors to insulators. We investigate other main group elements for their ability to form stable mono- or divalent anions by partly filling their valence p shell. Heavy elements with strong SOC show the potential to fill subshells of the p manifold and enable interesting band crossings. For Pb this can lead to a band gap, whereas the SOC is too small for lighter elements. Similarly, monovalent anions Bi^{1-} and Tl^{1-} can be used to create semiconducting systems with band gaps interesting for photovoltaic applications. We hope that the potential applications and the demonstrated

stability of some examples triggers experimental fabrication of IHPs in the near future.

Supporting Information Available

Structures (.cif) of the optimized structures in [Table 1](#).

Acknowledgement

This work was supported by the U.S. Office of Naval Research, under Grant N00014-17-1-2574. J. G. thanks the German Research Foundation for support from Research Fellowship GE 2827/1-1. Computational support is provided by the HPCMO of the U.S. DOD.

References

- (1) Gebhardt, J.; Rappe, A. M. Adding to the perovskite universe: inverse-hybrid perovskites. *ACS Energy Lett.* **2017**, *2*, 2681–2685.
- (2) He, T.; Huang, Q.; Ramirez, A. P.; Wang, Y.; Regan, K. A.; Rogado, N.; Hayward, M. A.; Haas, M. K.; Slusky, J. S.; Inumara, K. et al. Superconductivity in the non-oxide perovskite MgCNi_3 . *Nature* **2001**, *411*, 54–56.
- (3) Takenaka, K.; Takagi, H. Giant negative thermal expansion in Ge-doped anti-perovskite manganese nitrides. *Appl. Phys. Lett.* **2005**, *87*, 261902.
- (4) Kamishima, K.; Goto, T.; Nakagawa, H.; Miura, N.; Ohashi, M.; Mori, N.; Sasaki, T.; Kanomata, T. Giant magnetoresistance in the intermetallic compound Mn_3GaC . *Phys. Rev. B* **2000**, *63*, 024426.
- (5) Gäbler, F.; Schnelle, W.; Senyshyn, A.; Niewa, R. Magnetic structure of the inverse perovskite (Ce_3N) In. *Solid State Sci.* **2008**, *10*, 1910–1915.

- (6) Wang, B. S.; Tong, P.; Sun, Y. P.; Tang, W.; Li, L. J.; Zhu, X. B.; Yang, Z. R.; Song, W. H. Structural, magnetic properties and magnetocaloric effect in Ni-doped antiperovskite compounds $\text{GaCMn}_{3-x}\text{Ni}_x$ ($0 \leq x \leq 0.10$). *Phys. B* **2010**, *405*, 2427–2430.
- (7) Gomonaj, E. V.; L’Vov, V. A. A theory of spin reorientation and piezomagnetic effect in noncollinear Mn_3AgN antiferromagnet. *Phase Transitions* **1992**, *40*, 225–237.
- (8) Sun, Y.; Chen, X.-Q.; Yunoki, S.; Li, D.; Li, Y. New family of three-dimensional topological insulators with antiperovskite structure. *Phys. Rev. Lett.* **2010**, *105*, 216406.
- (9) Nuss, J.; Mühle, C.; Hayama, K.; Abdolazimi, V.; Takagi, H. Tilting structures in inverse perovskites, M_3TtO ($\text{M} = \text{Ca}, \text{Sr}, \text{Ba}, \text{Eu}$; $\text{Tt} = \text{Si}, \text{Ge}, \text{Sn}, \text{Pb}$). *Acta Crystallogr. Sect. B Struct. Sci. Cryst. Eng. Mater.* **2015**, *71*, 300–312.
- (10) Fang, H.; Jena, P. Super-ion inspired colorful hybrid perovskite solar cells. *J. Mater. Chem. A* **2016**, *4*, 4728–4737.
- (11) Fang, H.; Jena, P. Li-rich antiperovskite superionic conductors based on cluster ions. *Proc. Natl. Acad. Sci.* **2017**, *114*, 11046–11051.
- (12) Bremner, C. A.; Simpson, M.; Harrison, W. T. New molecular perovskites: cubic $\text{C}_4\text{N}_2\text{H}_{12} \cdot \text{NH}_4\text{Cl}_3 \cdot \text{H}_2\text{O}$ and 2-h hexagonal $\text{C}_6\text{N}_2\text{H}_{14} \cdot \text{NH}_4\text{Cl}_3$. *J. Am. Chem. Soc.* **2002**, *124*, 10960–10961.
- (13) Liu, G. Z.; Zhang, J.; Wang, L. Y. A novel molecular cubic perovskite built from charge-assisted hydrogen bond linkages. *Synth. React. Inorganic, Met. Nano-Metal Chem.* **2011**, *41*, 1091–1094.
- (14) Li, W.; Wang, Z.; Deschler, F.; Gao, S.; Friend, R. H.; Cheetham, A. K. Chemically diverse and multifunctional hybrid organiceinorganic perovskites. *Nat. Rev. Mater.* **2017**, *2*, 16099.

- (15) Xu, W.-J.; Du, Z.-Y.; Zhang, W.-X.; Chen, X.-M. Structural phase transitions in perovskite compounds based on diatomic or multiatomic bridges. *CrystEngComm* **2016**, *18*, 7915–7928.
- (16) Duan, Z.; Wang, Z.; Gao, S. Irreversible transformation of chiral to achiral polymorph of K [Co (HCOO)₃]: synthesis, structures, and magnetic properties. *Dalt. Trans.* **2011**, *40*, 4465–73.
- (17) Eikeland, E.; Lock, N.; Filsø, M.; Stingaciu, M.; Shen, Y.; Overgaard, J.; Iversen, B. B. Alkali metal ion templated transition metal formate framework materials: synthesis, crystal structures, ion migration, and magnetism. *Inorg. Chem.* **2014**, *53*, 10178–10188.
- (18) Thiele, G.; Messer, D. S-Thiocyanato- und N-isotrhiocyanato Bindungsisomerie in den Kristallstrukturen von RbCd (SCN), und CsCd (SCN),. *Zeitschrift für Anorg. und Allg. Chemie* **1980**, *464*, 255–267.
- (19) Perdew, J. P.; Burke, K.; Ernzerhof, M. Generalized gradient approximation made simple. *Phys. Rev. Lett.* **1996**, *77*, 3865–3868.
- (20) Giannozzi, P.; Baroni, S.; Bonini, N.; Calandra, M.; Car, R.; Cavazzoni, C.; Ceresoli, D.; Chiarotti, G. L.; Cococcioni, M.; Dabo, I. et al. QUANTUM ESPRESSO: a modular and open-source software project for quantum simulations of materials. *J. Phys. Condens. Matter* **2009**, *21*, 395502.
- (21) Grimme, S. Semiempirical GGA-type density functional constructed with a long-range dispersion correction. *J. Comput. Chem.* **2006**, *27*, 1787–1799.
- (22) Rappe, A. M. A.; Rabe, K. K. M.; Kaxiras, E.; Joannopoulos, J. D. J. Optimized pseudopotentials. *Phys. Rev. B* **1990**, *41*, 1227.
- (23) Ramer, N. J.; Rappe, A. M. Designed nonlocal pseudopotentials for enhanced transferability. *Phys. Rev. B* **1999**, *59*, 12471.

- (24) Grinberg, I.; Ramer, N.; Rappe, A. Transferable relativistic dirac-slater pseudopotentials. *Phys. Rev. B* **2000**, *62*, 2311–2314.
- (25) Monkhorst, H. J.; Pack, J. D. Special points for Brillouin-zone integrations. *Phys. Rev. B* **1976**, *13*, 5188–5192.
- (26) Krukau, A. V.; Vydrov, O. A.; Izmaylov, A. F.; Scuseria, G. E. Influence of the exchange screening parameter on the performance of screened hybrid functionals. *J. Chem. Phys.* **2006**, *125*, 224106.
- (27) Marzari, N.; Vanderbilt, D. Maximally localized generalized wannier functions for composite energy bands. *Phys. Rev. B* **1997**, *56*, 12847–12865.
- (28) Setyawan, W.; Curtarolo, S. High-throughput electronic band structure calculations: challenges and tools. *Comput. Mater. Sci.* **2010**, *49*, 299–312.
- (29) Goldschmidt, V. M. Die gesetze der Krystallochemie. *Naturwissenschaften* **1926**, *14*, 477–485.
- (30) Kieslich, G.; Sun, S.; Cheetham, A. K. Solid-State principles applied to organiceinorganic perovskites: new tricks for an old dog. *Chem. Sci.* **2014**, *5*, 4712–4715.
- (31) Travis, W.; Glover, E. N. K.; Bronstein, H.; Scanlon, D. O.; Palgrave, R. G. On the application of the tolerance factor to inorganic and hybrid halide perovskites: a revised system. *Chem. Sci.* **2016**, *7*, 4548–4556.
- (32) Shannon, R. D.; Prewitt, C. T. Effective ionic radii in oxides and fluorides. *Acta Cryst.* **1969**, *B25*, 925–946.
- (33) Shannon, R. D. Revised effective ionic radii and systematic studies of interatomic distances in halides and chalcogenides. *Acta Crystallogr., Sect A Cryst. Phys., Diffraction, Theor. Gen. Crystallogr.* **1976**, *32*, 751–767.

- (34) Jain, A.; Ong, S.; Hautier, G.; Chen, W.; Richards, W.; Dacek, S.; Cholia, S.; Gunter, D.; Skinner, D.; Ceder, G. et al. Materials project. 2016; <https://www.materialsproject.org>.
- (35) Gebhardt, J.; Rappe, A. M. Under review. **2018**,
- (36) Beberwyck, B. J.; Surendranath, Y.; Alivisatos, A. P. Cation exchange: A versatile tool for nanomaterials synthesis. *J. Phys. Chem. C* **2013**, *117*, 19759–19770.
- (37) Dye, J. L.; Ceraso, J. M.; Lok, M. T.; Barnett, B. L.; Tehan, F. J. A crystalline salt of the sodium anion (Na^-). *J. Am. Chem. Soc.* **1974**, *96*, 608–609.
- (38) Troyanov, S. I.; Krahll, T.; Kemnitz, E. Crystal structures of $\text{Ga}x_3(X=\text{Cl, Br, I})$ and AlI_3 . *Zeitschrift für Krist.* **2004**, *219*, 88–92.
- (39) Holleman, A. F.; Wiberg, E.; Wiberg, N. *Lehrbuch der Anorganischen Chemie*, 102nd ed.; de Gruyter: Berlin, 2007.
- (40) Wang, C.; Takenaka, K.; Li, L.; Sun, Y. Lattice and magnetic and electronic transport properties in antiperovskite M_3AX compounds. *Adv. Condens. Matter Phys.* **2013**, *2013*, 214120.
- (41) Stoumpos, C. C.; Frazer, L.; Clark, D. J.; Kim, Y. S.; Rhim, S. H.; Freeman, A. J.; Ketterson, J. B.; Jang, J. I.; Kanatzidis, M. G. Hybrid germanium iodide perovskite semiconductors: active lone pairs, structural distortions, direct and indirect energy gaps, and strong nonlinear optical properties. *J. Am. Chem. Soc.* **2015**, *137*, 6804–6819.
- (42) The National Institute for Occupational Safety and Health (NIOSH), Lead. 2016; <https://www.cdc.gov/niosh/npg/npgd0368.html>.
- (43) Nakajima, T.; Sawada, K. Discovery of Pb-free perovskite solar cells via high-throughput simulation on the K computer. *J. Phys. Chem. Lett.* **2017**, *8*, 4826–4831.

- (44) The National Institute for Occupational Safety and Health (NIOSH), Thallium, soluble compounds (as Tl). 2004; <https://www.cdc.gov/niosh/npg/npgd0608.html>.
- (45) Yamamuro, O.; Matsuo, T.; Suga, H.; David, W. I. F.; Ibberson, R. M.; Leadbetter, A. J. Neutron diffraction and calorimetric studies of methylammonium iodide. *Acta Cryst.* **1992**, *B48*, 329–336.
- (46) Gabe, E. J. The crystal structure of methyl ammonium bromide. *Acta. Cryst.* **1961**, *14*, 1296.
- (47) Hughes, E. W.; Lipscomb, W. N. The crystal structure of methylammonium chloride. *J. Am. Chem. Soc.* **1946**, *68*, 1970–1975.
- (48) Lux, D.; Schwarz, W.; Hess, H. Methylammonium fluoride, $\text{CH}_3\text{NH}_3\text{F}$. *Cryst. Struct. Commun.* **1979**, *8*, 41–43.

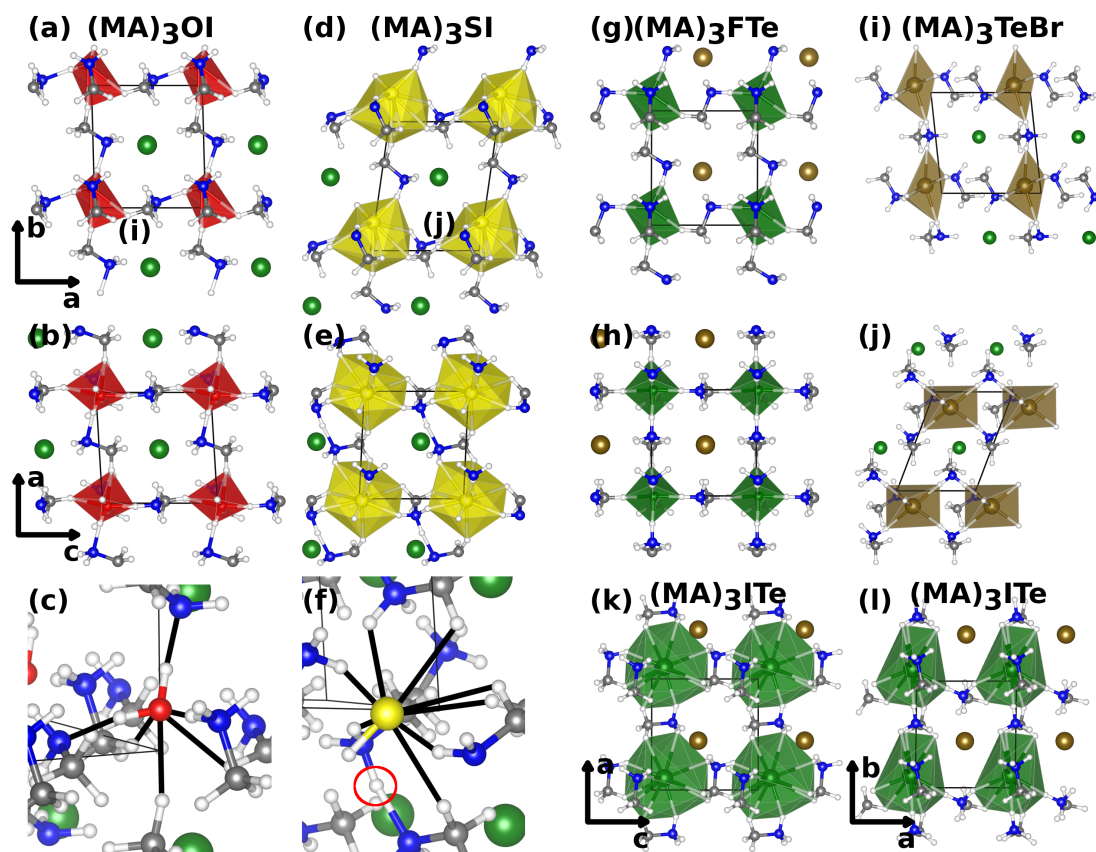


Figure 1: Representative structures of IHPs. Atoms are colored gray (C), blue (N), white (H), red (O), yellow (S), green (halogens), and brown (Se or Te). Colored polyhedra indicate $B-H$ bonding. (a - f) show perovskite structures with B -site protonation. $(MA)_3FTe$ as exemplary IHP structure with head-on $B \cdots X \cdots B$ bonding motif is shown in (g, h). For $t < 0.76$, the alternative $CaIrO_3$ phase (i, j) is observed for most cases. In the perovskite structure, small t leads to a rotation of MA units from the head-on to a side-on structure P_{\perp} (k, l). (c) and (f) show a close up on a (protonated) B -site for O and S, respectively. Only covalent $B-H$ bonds are drawn; hydrogen bonds are indicated by black lines. In (c), the central O has two short O-H bonds and is generally displaced off-center towards three NH_3 groups. In (f), MA units are tilted side-on and two MA units share one H (red circle). One H is detached from MA, forming an S-H bond, oriented towards a BX_3 plane.

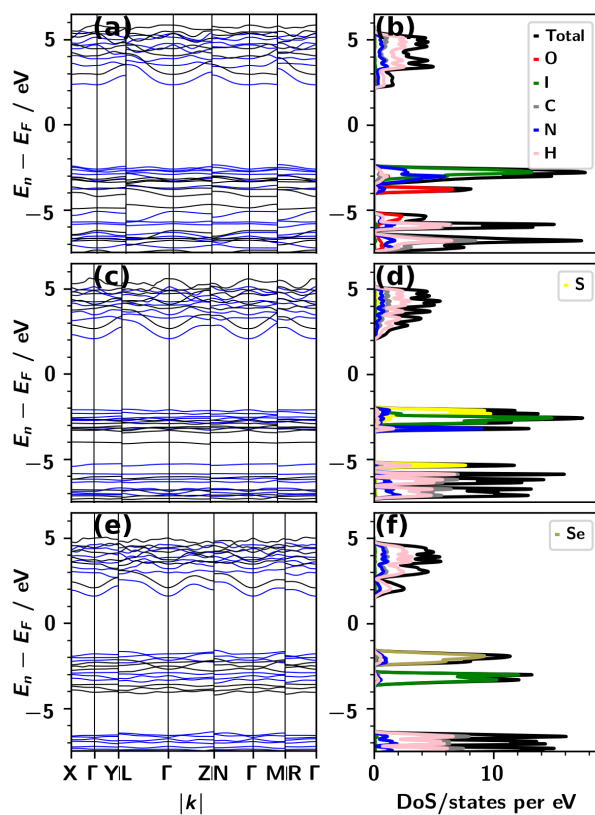


Figure 2: Band structure and DoS for $(\text{CH}_3\text{NH}_3^+)(\text{CH}_3\text{NH}_2)_2(\text{H}_2\text{O})\text{I}^-$ (a, b), $(\text{CH}_3\text{NH}_3^+)_2(\text{CH}_3\text{NH}_2)(\text{HS}^-)\text{I}$ (c, d), and $(\text{MA})_3\text{SeI}$ (e, f). Bands are colored according to elemental species in Fig. 1 and H in pink for visibility. VB and CB regions are dominated by anion and cation contributions, respectively. In the O case, cation orbitals mix more strongly with anion orbitals, due to the formation of water and the resulting hydrogen-bonded network. The relative alignment of bands from the anion sites changes with the ion composition, allowing to tune the gap of these wide band-gap semiconductors. For a better quantitative estimate of the band gap, we compare the PBE band structures (blue) with HSE calculations (black).

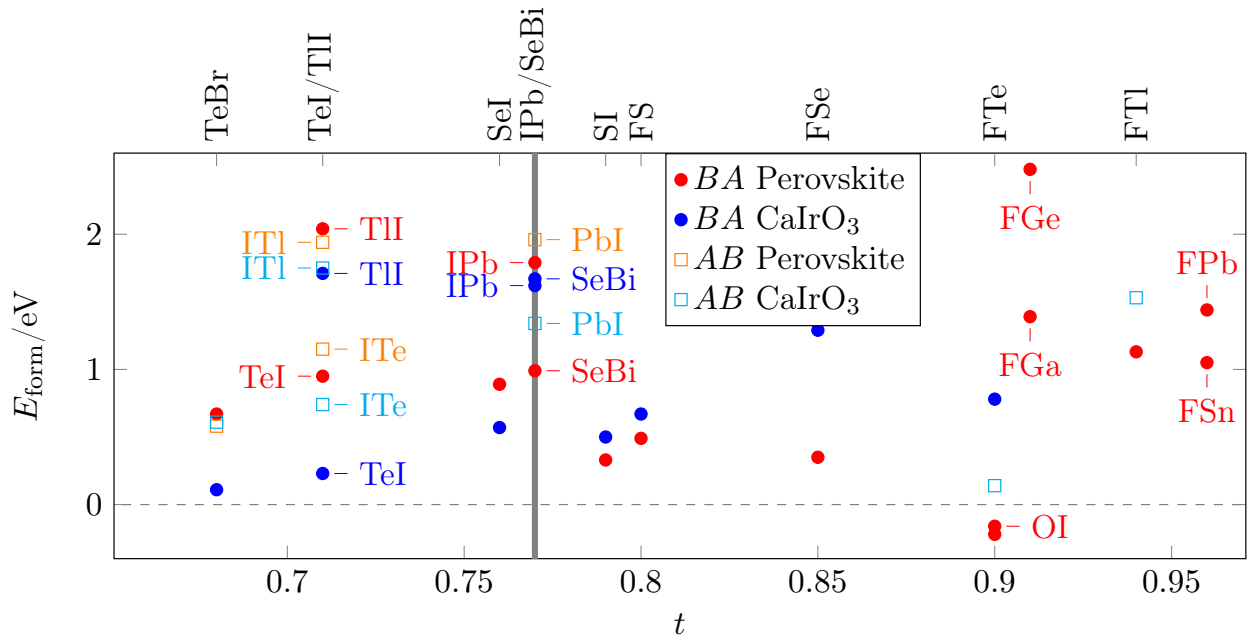


Figure 3: Formation energies of the perovskite (red) and the CaIrO_3 phase (blue) for the investigated $(\text{MA})_3\text{BA}$ IHPs. The perovskite structure is favored for $t > 0.76$. For smaller values, the CaIrO_3 structure becomes more stable. The energetic preference between both phases is in line with the computed tolerance factors. Stability and site preference with respect to anion location is shown by comparing with the respective $X_3\text{AB}$ compounds for some cases, displaying the perovskite (orange) and CaIrO_3 (cyan) phases.

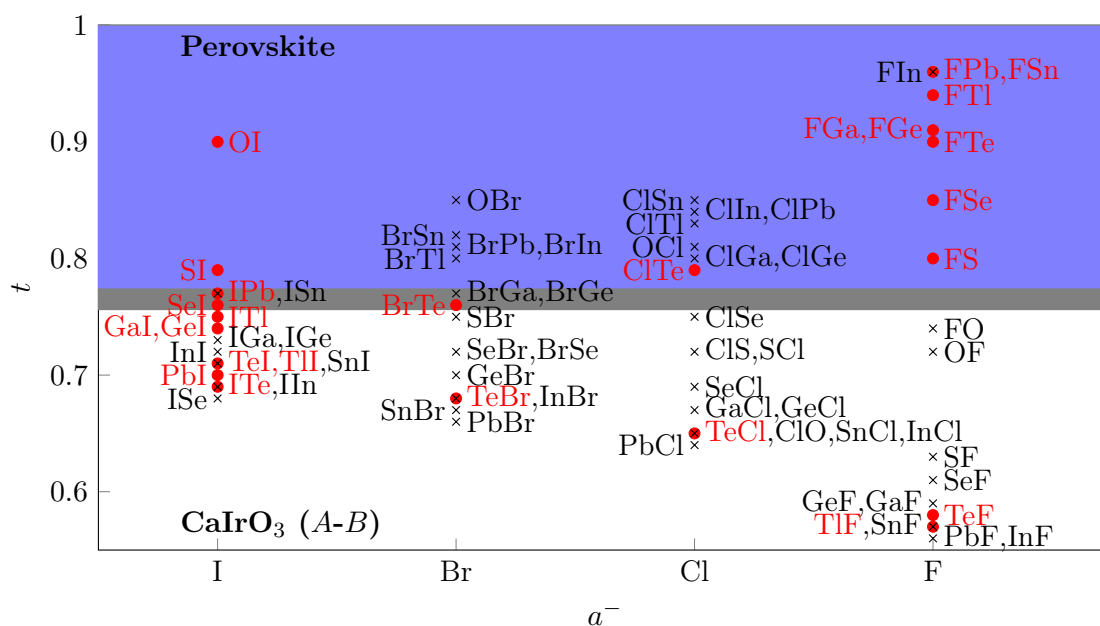


Figure 4: Estimated tolerance factors for $(\text{MA})_3\text{BA}$ IHP halides. Computed structures where the stability of the perovskite structure was compared to other phases are marked red, possible other compounds that were not computed explicitly black. Perovskites are found for $t > 0.76$ (blue region). For $t < 0.76$ we observe a different phase (CaIrO_3). In this region, a few unstable cases lead to deformed structures with zig-zag shaped A - B bonds (often accompanied by protonation). At $t = 0.76$ and a small intermediate region (gray region), both phases and particularly distorted structures are observed.

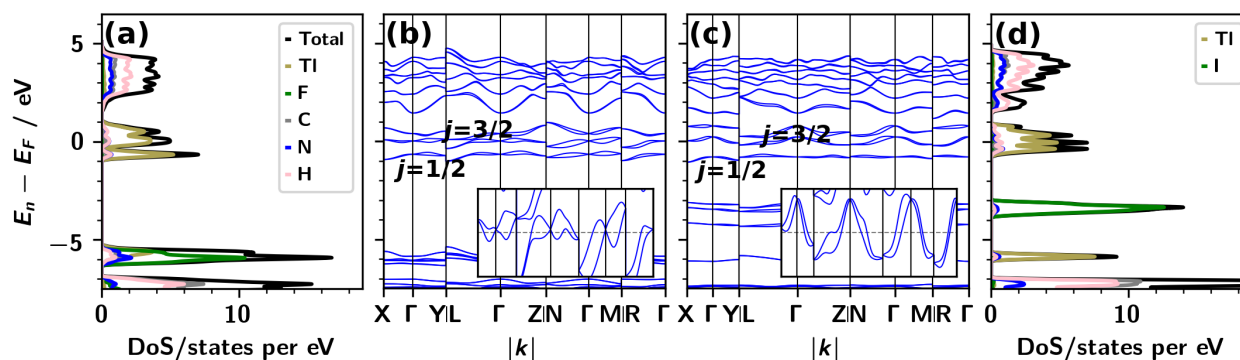


Figure 5: DoS (a) and band structure (b) of MA_3FTl . The valence p shell is located around the Fermi level. Three valence electrons of the Tl^{2-} ion lead to a fractional filling of the lower pair of $j = 3/2$ bands and a metallic band structure. Despite the phase change (CaIrO_3), $(\text{MA})_3\text{TlI}$ has similar electronic structure (c, d). The I valence p bands are observed at higher energies compared to the F bands, effectively decoupling them from the Tl s band. Insets in (b, c) show a close-up of the bands around the Fermi level (dashed gray line).

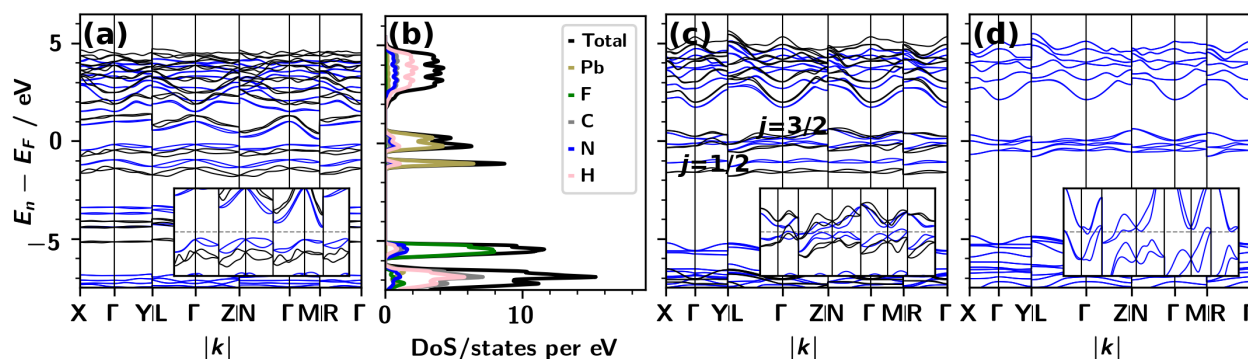


Figure 6: Band structures of (a) $(\text{MA})_3\text{IPb}$, (c) $(\text{MA})_3\text{FPb}$, and (d) $(\text{MA})_3\text{FSn}$. In addition, for $(\text{MA})_3\text{FPb}$ the DoS is shown in (b). Blue and black bands show PBE and HSE bands, respectively. Close-ups show the $j=3/2$ bands around the Fermi level (dashed gray line). While a small gap is observed in (a) throughout the BZ, the fluoride compounds are metallic.

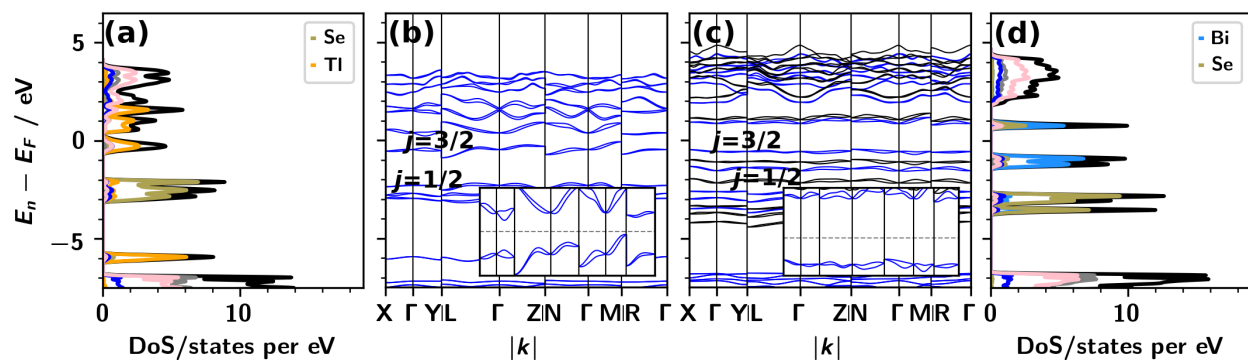


Figure 7: DoS and band structure for $(\text{MA})_3\text{SeTl}$ (a, b) and $(\text{MA})_3\text{SeBi}$ (c, d). A band gap is introduced between valence $p\ j=1/2$ and $j=3/2$ bands (b) or between the two pairs of $j=3/2$ bands (c).

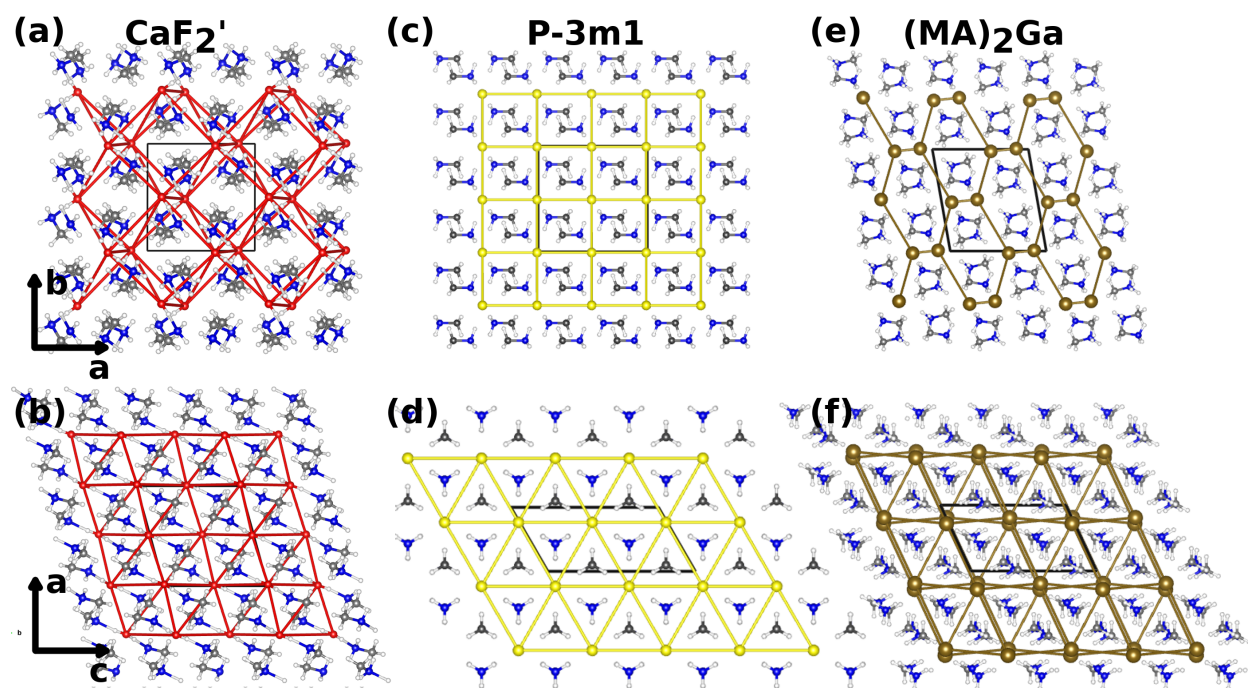
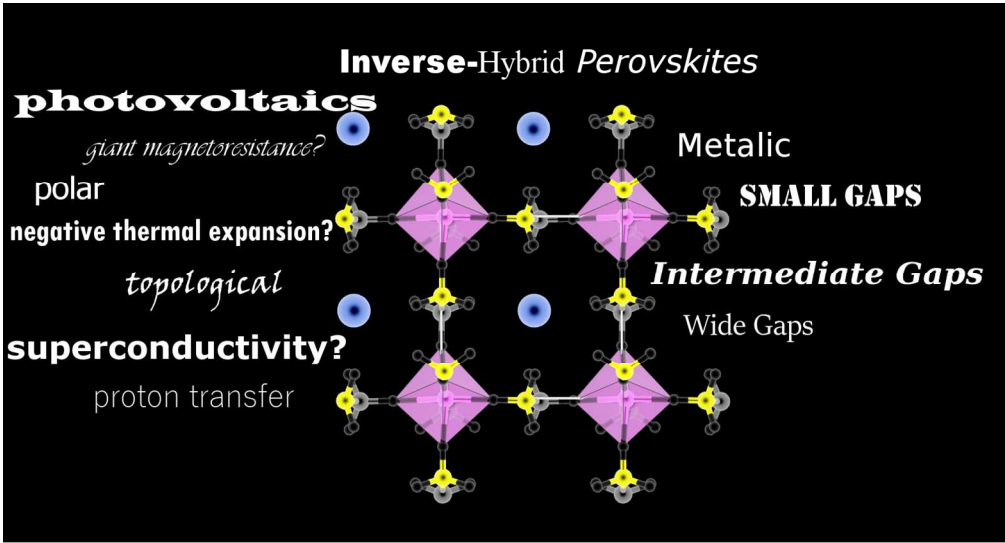


Figure 8: Exemplary structures of $(MA)_2a^{2-}$ compounds: (a) distorted CaF_2 structure for O, (b) trigonal phase for S (representative for Se, Te, Sn, and Pb), (c) intermediate phase for Ga (representative for Tl and Ge).



554x298mm (72 x 72 DPI)